



# Development of a MWDC prototype of the CSR external-target experiment

Zhou-Bo He<sup>1,2</sup> · Zhi Qin<sup>3</sup> · Peng Ma<sup>1,2</sup> · He-Run Yang<sup>1,2</sup> · Xiang-Lun Wei<sup>1,2</sup> · Chen-Gui Lu<sup>1,2</sup> · Xiang-Jie Wen<sup>1,2</sup> · Xiu-Ling Zhang<sup>1,2</sup> · Tao Chen<sup>4</sup> · Zhi-Jie Li<sup>1,2</sup> · Yuan-Sheng Yang<sup>1,2</sup> · Mei-Qiang Zhan<sup>5</sup> · Can-Wen Liu<sup>3</sup> · Meng Li<sup>1,2</sup> · Tian-Li Qiu<sup>1,2</sup> · Yi-Wei Gong<sup>1,2</sup> · Xin-Jie Huang<sup>1,2</sup> · Xiao-Hao Yin<sup>1,2</sup> · Zhi-Xuan He<sup>6</sup> · Jun-Wei Zhang<sup>7</sup> · Hai-Chuan Zou<sup>1</sup> · Sheng-Wei Fu<sup>1,2</sup> · Dong Guo<sup>3</sup> · Jun-Wei Yan<sup>1,2</sup> · Zhe Cao<sup>4</sup> · Zhi Deng<sup>3</sup> · Jie Kong<sup>1,2</sup> · Zhi-Gang Xiao<sup>3</sup> · Rong-Jiang Hu<sup>1,2</sup> · Li-Min Duan<sup>1,2</sup>

Received: 30 November 2023 / Revised: 4 January 2024 / Accepted: 18 January 2024 / Published online: 24 September 2024  
© The Author(s), under exclusive licence to China Science Publishing & Media Ltd. (Science Press), Shanghai Institute of Applied Physics, the Chinese Academy of Sciences, Chinese Nuclear Society 2024

## Abstract

The cooling storage ring (CSR) external-target experiment (CEE) is a spectrometer used in construction to study the properties of nuclear matter in high-baryon density regions at the Heavy-Ion Research Facility in Lanzhou (HIRFL). This study presents the design, simulation, manufacturing, and testing of a half-size prototype of a multi-wire drift chamber (MWDC) for the CEE. First, the performance of the MWDC connected to homemade electronics was simulated. The results demonstrated that an energy resolution of 18.5% for 5.9-keV X-rays and a position resolution of 194  $\mu\text{m}$  for protons can be achieved by the current design. Because the size of the largest MWDC reached 176 cm  $\times$  314 cm, a set of 98 cm  $\times$  98 cm prototypes was built using the new techniques. The positioning accuracy of the anode wires in this prototype is better than 20  $\mu\text{m}$ . After optimization, using commercially available electronics, the prototype can achieved an energy resolution of 19.7% for a  $^{55}\text{Fe}$  X-ray source. The CEE-MWDC detector and electronics were simultaneously tested. An energy resolution of 22% was achieved for the  $^{55}\text{Fe}$  source; the track residuals were approximately 330  $\mu\text{m}$  for the cosmic rays. The results demonstrate that the current design and techniques meet the requirements of the CEE-MWDC array.

**Keywords** CEE · MWDC · Garfield++ ·  $^{55}\text{Fe}$  source · Position resolution

Zhou-Bo He, Zhi Qin have contributed equally to this work.

This work was supported by the Research Program of the National Major Research Instruments (No. 11927901), Strategic Priority Research Program of the Chinese Academy of Sciences (No. XDB34000000), National Key R & D Program of China (No. 2018YFE0205200), Natural Science Foundation of China (Nos. 11875301, 11875302, U1867214, U1832105, U1832167), CAS "Light of West China" Program, and the Function Development Project of Chinese Academy of Sciences (No. 2022G101).

✉ Rong-Jiang Hu  
hurj@impcas.ac.cn

✉ Li-Min Duan  
lmduan@impcas.ac.cn

<sup>1</sup> Institute of Modern Physics, Chinese Academy of Sciences, Lanzhou 730000, China

<sup>2</sup> School of Nuclear Science and Technology, University of Chinese Academy of Sciences, Beijing 100049, China

<sup>3</sup> Department of Physics, Tsinghua University, Beijing 100084, China

## 1 Introduction

Experiments regarding heavy-ion collisions are conducted to study the equation of state of nuclear matter (nEOS). Compressed nuclear matter beyond the saturation density can be created in the energy region ranging from hundreds of MeV/u to 1 GeV/u. EOS constraints of nuclear matter

<sup>4</sup> University of Science and Technology of China, Hefei 230026, China

<sup>5</sup> Key Laboratory of Radiation Physics and Technology of the Ministry of Education, Institute of Nuclear Science and Technology, Sichuan University, Chengdu 610064, China

<sup>6</sup> School of Nuclear Science and Technology, Lanzhou University, Lanzhou 730000, China

<sup>7</sup> North China University of Water Resources and Electric Power, Zhengzhou 450000, China

can be determined by using the observables identified in heavy-ion experiments. Several heavy-ion experiments have been operated or are currently running worldwide.

The cooling storage ring (CSR) at the heavy-ion research facility at Lanzhou (HIRFL) provides beams from proton to uranium with a maximum energy of 2.8 GeV/u and 0.5 GeV/u, respectively [1–3]. In this energy region, nuclear stopping, defined as the ratio of the transverse energy to the longitudinal energy of the products in central heavy-ion collisions, reaches the maximum plateau, offering a beneficial opportunity to study the nEOS at approximately twice the saturation density [4, 5]. To utilize the beam conditions on the machine, the HIRFL-CSR external-target experiment (CEE) [6] was constructed in 2020. It is a multipurpose spectrometer that covers the entire solid angle at the center of the mass reference frame. It is designed to study the nEOS by measuring the phase space distribution of light-charged particles, flow observables, meson production, and correlation functions [7, 8].

Similar to many spectrometers worldwide, the key components of CEE include the tracking detectors placed in the magnetic field. In the forward region, the tracking array consists of three multi-wire drift chambers (MWDCs) that record the hits of the tracks emitted in the angular range from  $5^\circ$  to  $30^\circ$ .

In this study, we report the design, assembly, and testing of a half-sized prototype of the MWDC. Section 2 describes the design of CEE and the geometric setup of the MWDC array. Section 3 presents the simulation results for the joint performance of the CEE-MWDC detector and the front-end electronics. Section 4 introduces the prototype design and assembly. Section 5 describes the prototype-performance optimization process. Section 6 presents

the joint-testing results of the CEE-MWDC detector and electronics.

## 2 Main features of the CEE and its MWDC tracking array

The main component of the CEE is a large-gap magnetic dipole housing the tracking detectors. Figure 1a presents a schematic of the CEE spectrometer. The charged products at midrapidity, namely from  $30^\circ$  to  $110^\circ$  in the laboratory, were measured using a time projection chamber (TPC) [9, 10] surrounded by inner TOF walls (iTOF) [11]. Three MWDCs were installed perpendicular to the beam for charged particles emitted at forward angles [12–14], among which two were placed inside the field and one at the exit of the dipole. An end-cap TOF (eTOF) wall [15, 16] was placed downstream of the MWDC; the zero-degree counters (ZDC) were further out [17, 18]. All TOF detectors are multi-gap resistive plate counters (MRPCs) that deliver precise timing information when particles pass through the detector. The starting time is provided by the T0 detector [19, 20]. The beam spot is monitored using a silicon pixel detector based on top-metal techniques [21–23]. Details regarding the physical programs and design of the CEE can be found in [Guo et al., Eur. Phys. J. A, 2024] [24].

The eTOF and MWDC were used for particle identification in the small-angle region ( $5^\circ - 30^\circ$ ). Certain important parameters and performance indices of the CEE-MWDC are listed in Table 1. In the fixed-target experiment, the collision products of CEE were dominant in the forward region. Therefore, the particle identification (PID) ability in the forward hemisphere region of the laboratory system should be

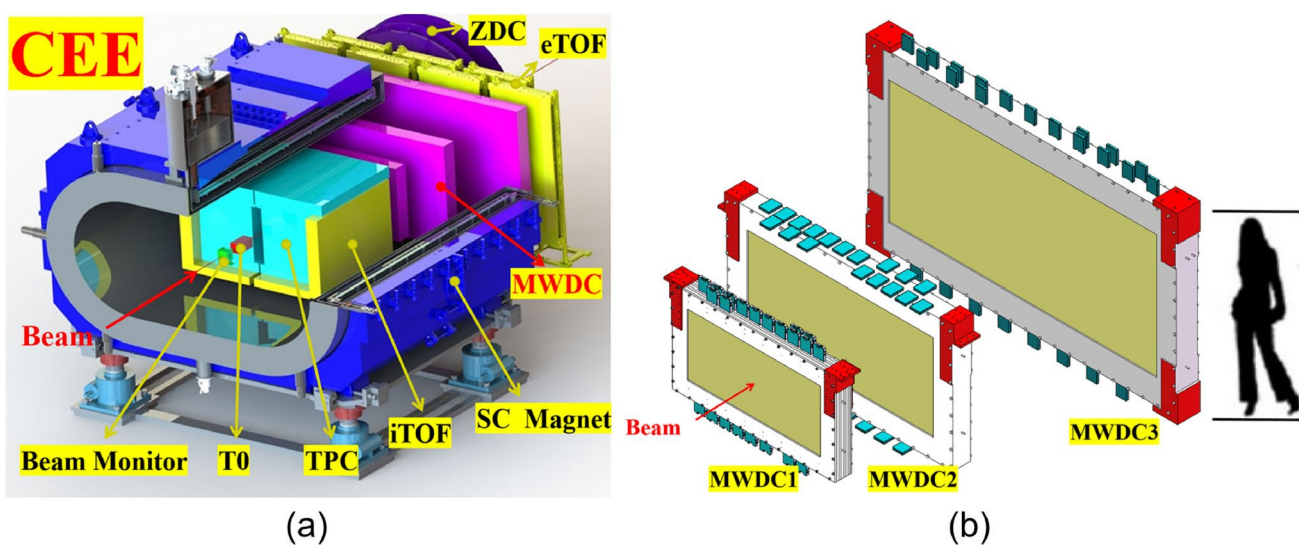


**Fig. 1** (Color online) **a** Schematic layout of the CEE spectrometer; **b** schematic layout of the MWDC array

**Table 1** CEE requirements for the MWDCs and prototype achievements

Item	Indices of the CEE-MWDC	Achievements in the prototype phase
Number of detectors	3	1 (Determined the design and fabrication process for large MWDC)
Minimum acceptance angle	5°	< 5° (MWDC array sizes determined by simulation)
Maximum acceptance angle	30°	> 30° (MWDC array sizes determined by simulation)
Energy resolution	< 22% (for 5.9-keV X-rays)	< 22% (for 5.9-keV X-rays)
Position resolution	< 300 $\mu\text{m}$ (for 300 MeV proton)	< 330 $\mu\text{m}$ (for cosmic rays)
Number of channels	Approximately 3000	384
Gain (For FEE)	1 mV/fC	1 mV/fC
Electronics system noise	5 fC	< 5 fC
Peak time of waveform (For FEE)	80 ns	80 ns or 160ns or 1 $\mu\text{s}$ (selectable)
Waveform sampling period (For SCA)	12.5 ns	12.5 ns
Dynamic range of electronics system	10 fC–900 fC	3 fC–1000 fC
Maximum allowable trigger rate	10 kHz	10 kHz

focused on. In the current design, although TPC can measure tracks with a relatively good momentum resolution, the efficiency and resolution in the forward region are insufficient [6]. Thus, a complementary tracking array consisting of MWDCs in the forward region is proposed owing to its many advantages including the cost, position resolution, and highest allowable count rate.

To maximize the acceptance of the MWDC array, the CEE spectrometer was equipped with three sets of MWDC detectors, two of which were placed on the dipole. The beam passed directly through the central area of the three sets of the MWDC. Figure 1b presents the design of the MWDC array. MWDC1, MWDC2, and MWDC3 were 93 cm  $\times$  166 cm, 128 cm  $\times$  230 cm, and 176 cm  $\times$  314 cm in size, respectively. The fabrication process and techniques for such large drift chambers must be tested; therefore, a 98 cm  $\times$  98 cm prototype set with a 384-channel readout was developed, which utilized several practical designs to verify the feasibility of building a large MWDC.

The electronics used for the MWDC detectors were homemade. FEAM chips were used in the integrated front-end electronics (FEE) to amplify and shape the input signals. Switched capacitor array (SCA) boards were developed to sample and digitize the waveforms. To avoid data congestion, the MWDC readout system utilized FPGAs to fit the waveform data online in real-time and extract the time and energy information.

### 3 Performance simulation of the CEE-MWDC prototype

#### 3.1 Garfield++

To verify the performance of the entire system, detailed simulations based on the Garfield++ [25] software were conducted, considering both the detector structure and front-end electronic responses.

Garfield++ is a software dedicated for the simulation of gas and semiconductor detectors. It can simulate particle-gas interactions, electron and ion drift processes in gases, and electron avalanche multiplication processes under strong electric fields. By simulating the drift of electrons and ions, the induced currents can be generated at the corresponding electrodes. A near-real signal waveform is then computed by applying the transfer function of the front-end electronics to the induced currents. The entire procedure integrates many programs, including HEED [26] to simulate the interaction between the rays and gas, and the Magboltz [27] to simulate the macroscopic parameters of the electron transport in gas, such as the drift velocity and Townsend coefficient. It includes the following three methods of electron and ion transport: Runge–Kutta–Fehlberg integration, Monte Carlo integration, and Avalanche-Microscopy. Both Runge–Kutta–Fehlberg and Monte Carlo integrations rely on the macroscopic parameters of electron transport in the corresponding gas simulated by the Magboltz program when simulating the electron transport paths in the gas and electron avalanche amplification process. To accurately simulate the electron trajectories in small-scale structures (with characteristic dimensions comparable to the mean free range of electrons) and for detailed calculations of the ionization and excitation processes, the microscopic tracking of electrons is simulated with Avalanche-Microscopy, which is used to

simulate the microscopic collisions of electrons with atoms to obtain the electron drift paths and avalanche amplification process. The simulations of the collisions are based on the data of the cross sections of electrons in each scattering process in MediumMagboltz (Magboltz 11.17 [28] contains all relevant cross sections of electron-matter interactions).

## 3.2 Simulation of energy resolution

### 3.2.1 Simulation process

Because the MWDC consists of numerous drift cells, a simplified model was used for performance simulations. The model retains the windows and wires of adjacent cells to simulate the signal generation process of a single cell. It can extract the relevant amplitude and time information from the waveform of the signal, thus obtaining the energy and position resolutions of a single drifting cell of the MWDC. The cell size of the prototype was planned to be 10 mm × 10 mm; therefore, the model size of the simulated drift cell was set to 10 mm × 10 mm, and the cathode wire spacing was 2.5 mm. The 5.9-keV X-rays from a  $^{55}\text{Fe}$  source are often used to test the energy resolution of gas detectors with amplification. The HEED program was used to simulate the ionization excitation process of 5.9-keV X-rays with the corresponding gas. An example of the spatial-position distribution of primary electrons produced by the absorption of a 5.9-keV X-ray in the working gas is shown in Fig. 2. The electrons produced by the reaction included one photoelectron at 2.694 keV, one Auger electron at 2.709 keV, and two Auger electrons at 0.217 keV [29]. These electrons continue to ionize the gas to produce secondary electrons.

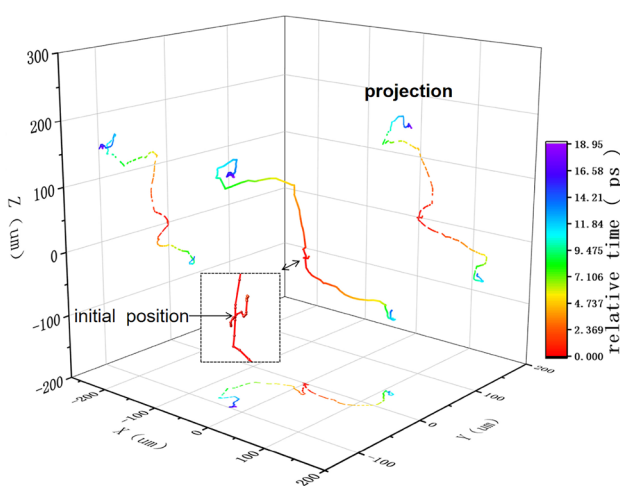


**Fig. 2** (Color online) Spatial paths of conductive (primary) electrons generated by the absorption of an X-ray with an energy of 5.9 keV in the argon atom of the gas mixture. (Only one event is displayed as an example.)

The spatial-position distribution of the primary electrons is generally near 200  $\mu\text{m}$ . The AvalancheMicroscopic method was used to simulate the corresponding electron drift and avalanche processes, and the Monte Carlo integration method was used to simulate the ion transport process. A combination of these two methods can accurately simulate the charge transport process. An accurate simulation of the electron avalanche process, as well as the electron and ion transport processes, can improve the accuracy of the simulated induced current of the electrode. The following gas parameters were set in the simulation: composition of 20%  $\text{CO}_2$  and 80% Ar, air pressure of 0.85 atm (matching the local air pressure), and temperature of 25  $^\circ\text{C}$  (matching the ambient temperature). Certain important parameters of the CEE-MWDC electronic system are listed in Table 1. The induced current on the anode must be convolved with the transfer function of the front-end electronics (FEE) to obtain the final signal waveform. The signal generated by the pulse generator was fed into the FEE, and the oscilloscope sampled the FEE output waveform. Garfield++ software reads the output waveform file and calculates it to obtain the transfer function of the front-end electronics.

### 3.2.2 Simulation results

The signal waveform of a 5.9-keV X-ray captured by the oscilloscope is shown in Fig. 3a, and that simulated by Garfield++ is shown in Fig. 3b, which superimposes the baseline noise with a peak-to-peak value of approximately 10 mV.

A total of 6000 signal waveforms of the 5.9-keV X-rays were simulated to obtain the energy spectrum, the results of which are shown in Fig. 4a. These X-rays were uniformly incident on the drift cell in the direction of the anode wire. The anode voltage was +1500 V, and that of the cathode and field wires was 0 V. The full energy peak of the energy spectrum was 209.5 mV, with an energy resolution of approximately 18.5%, which meets the requirement of CEE. The energy resolution included the contributions of the fluctuations in the primary ionization, fluctuations in the avalanche amplification gain, and noise with a peak-to-peak value of 10 mV. The experimental spectrum of the  $^{55}\text{Fe}$  source test is shown in Fig. 4b. The experimental results were apparently worse than those of the simulation, which is mainly owing to the fact that the simulation was more ideal. In fact, the surface inhomogeneity of the MWDC anode wire, nonlinearity of the electronic system, and waveform sampling frequency of the SCA reduced the energy resolution to a certain extent. In addition, the noise was greater in the experiment than in the simulation. Furthermore, there was a significant cosmic-ray background in the experimental energy spectrum compared with that of the simulated energy.

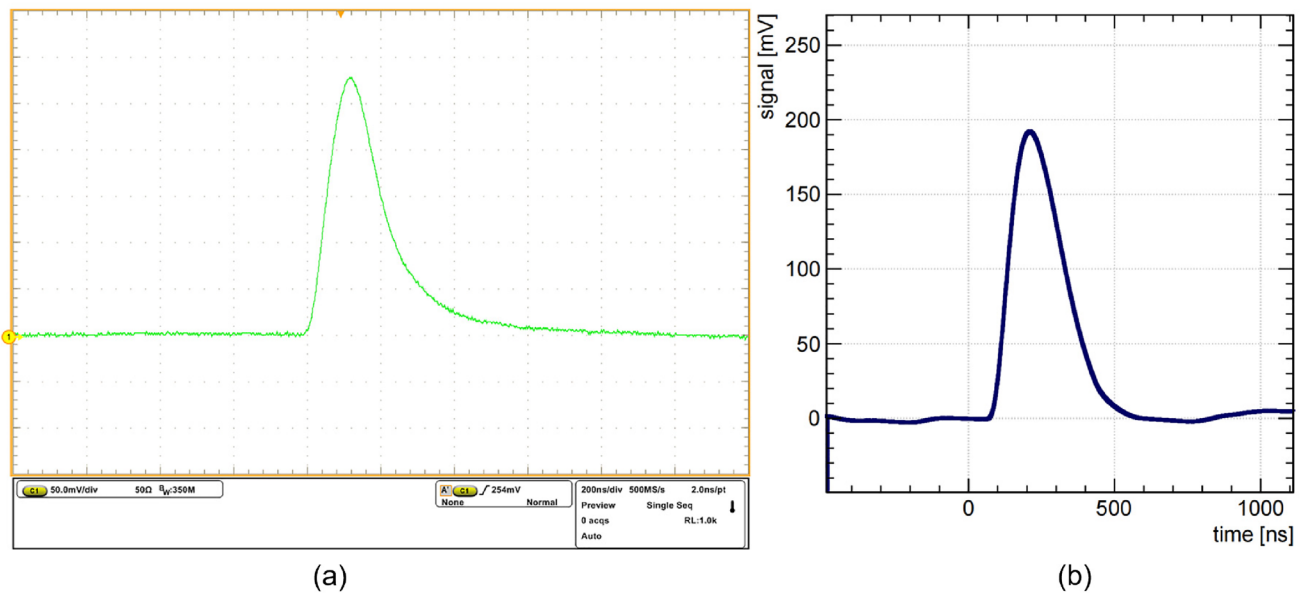


**Fig. 3** **a** Waveform captured by the oscilloscope in the experiment; **b** simulated waveform under the same conditions

The anode signal amplitude and electron avalanche gain were simulated as functions of the operating voltage, as shown in Fig. 4c. The gain and amplitude increased as the voltage increased, and the rate of increase became more pronounced at high voltages. The simulation results generally agree with the experimental results.

### 3.3 Simulation of position resolution

First, the electron drift isochrones of the drift cell in this structure were simulated, as shown in Fig. 5a. Generally, if the drift isochrones of the electrons are closer to a circle, the position resolution of the detector will be better; however, the final position resolution of the detector was determined by the detector connected to the electronics.

The simulation conditions for the position resolution were set in the same manner as that used for the energy resolution simulation. The position resolution of the prototype was simulated for muons with a momentum ranging from 1 GeV/c to 1 TeV/c. The corresponding operating voltage of the detector was 1550 V. The incidence angles of the muons were uniformly distributed in the interval ranging from 0° to 30°. Approximately 20000 effective muon tracks were randomly generated for the simulation. The signal waveform generated after each muon crossed the drift cell was simulated; the electron drift time spectrum of all the muons obtained using the constant ratio timing method with a trigger ratio of 0.5 is shown in Fig. 6a. A Fermi–Dirac function was used to fit the leading edge of the drift time spectrum and to obtain the drift starting time ( $T_0$ ) of the electrons [30]. The electron drift time ( $T$ ) was calculated with respect to  $T_0$ . The distance

( $R$ ) from the muon track-to-the anode wire is a known input parameter. The  $R$ – $T$  function was obtained by creating an  $R$ – $T$  correlation plot of all the muon tracks and conducting a fit. The  $R$ – $T$  correlation plot of the muons for the six sets of incidence angle intervals is shown in Fig. 6c. The  $R$ – $T$  function obtained by fitting the  $R$ – $T$  correlation plot is shown in Fig. 6b. The simulation results demonstrate a large difference in the  $RT$  functions corresponding to different angles at more than 50 ns. The simulated electron drift time ( $T$ ) of each track was incorporated into the  $R$ – $T$  relationship to obtain the fitted spatial distance ( $R$ -fit). The difference between the  $R$ -fit and real track-to-the anode wire distance ( $R$ ) is the track residual. The distribution of the track residuals for approximately 20000 muons is shown in Fig. 6d. Typically, the position resolution of an MWDC significantly deteriorates when charged particles pass near the anode wire or drift cell boundaries. Therefore, the residual distribution was fitted with a double Gaussian function [31], resulting in a corresponding position resolution of 348  $\mu\text{m}$ . The position resolution of the prototype was simulated for protons with a momentum ranging from 0.1 to 10 GeV/c. The corresponding operating voltage of the detector was 1400 V. As shown in Fig. 6e, the position resolution (sigma) was 194  $\mu\text{m}$ , satisfying the CEE requirements. The position resolution of the CEE-MWDC for the protons was significantly better than that of the high-energy muons, which is owing to the fact that the primary electrons produced by the ionization of protons in the gas are more uniform and regular. Although the position of the primary electrons of the protons has less of a negative impact, the signal waveform of the protons is more ideal.

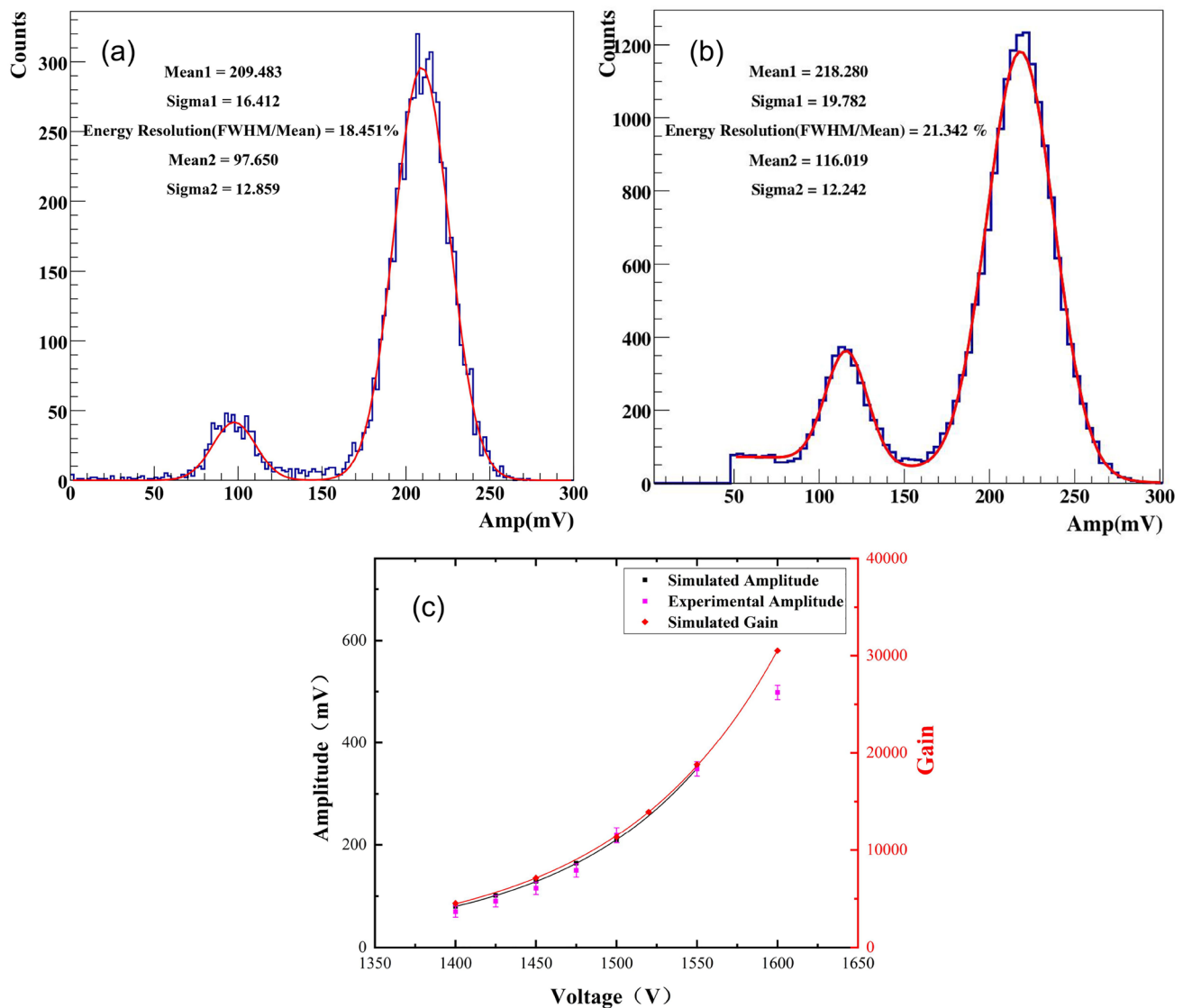


**Fig. 4** **a** Simulated energy spectrum of 5.9-keV X-rays; **b** energy spectrum of the  $^{55}\text{Fe}$  source measured in the experiment; **c** experimental and simulated signal amplitudes of the 5.9-keV X-rays as a function of the operating voltage

## 4 Development of CEE-MWDC prototype

### 4.1 Design details

To maximize the reception of the MWDC array of the reaction products, the CEE spectrometer uses three sets of MWDC detectors. The beam passed directly through the center of the detector. To maintain the same acceptance, the size of the chamber most downstream from the target was 176 cm  $\times$  314 cm. Therefore, the process of creating a chamber with such a large drift must be further explored. The performance was tested and compared with the simulation results presented in Sect. 2. Therefore, a 98 cm  $\times$  98 cm prototype set was designed and built to verify the process of building a large drift chamber. As shown in Fig. 7a,

the detector includes X, U, and V measurement layers, an entrance window, and an exit window. The windows were composed of 50- $\mu\text{m}$  thick double-sided aluminum-coated Kapton foil. Each measurement layer included two layers of anode wires and three layers of cathode wires. To measure the three-dimensional track of the particles, the wires of the X, U, and V layers were along the vertical direction, at an angle of  $-30^\circ$  to the wires of the X layer, and at an angle of  $30^\circ$  to the wires of the X layer, respectively. For each direction of the wires, to discriminate between the left and right positions, the anode wires mounted in two adjacent layers were displaced by 5 mm. For the ease of fabrication and maintenance, the X, U, and V layers were completely independent. In addition, the three layers can be assembled into an entire detector by using a sealing ring. In

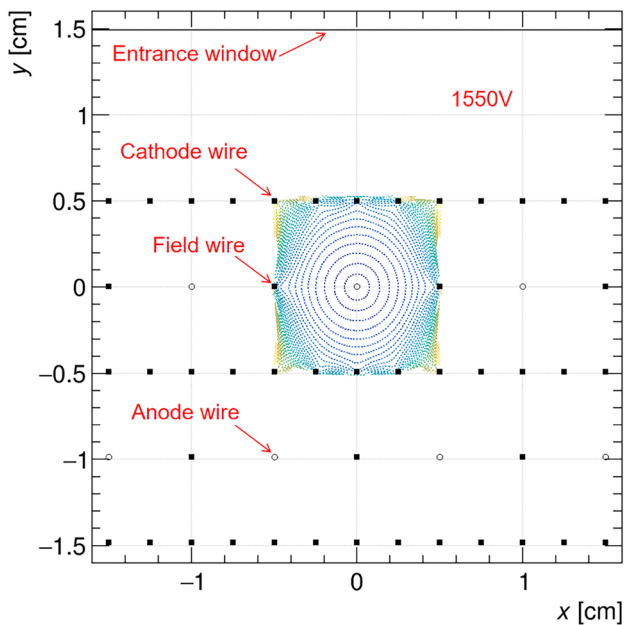


**Fig. 5** (Color online) Electron drift isochrones of a drift cell (Contour interval = 10 ns, HV = +1550 V, simulated by Garfield++)

addition, to minimize the maintenance costs, each measurement layer was designed with a partitioned structure. As shown in Fig. 7b, the sensitive area of the X-measurement layer is divided into four zones, and the mechanical, PCB, and signal lead components of each partition are completely independent.

Figure 7c shows the cross section of the X-measurement layer. Each measurement layer consisted of four main parts: a bottom support frame, bounding wall, layer-spacing control pad, and PCB. For a large MWDC, it is essential to resolve the structural deformation caused by the significant wire tension. Therefore, a 20-mm thick aluminum alloy was used as the support frame in the prototype, which avoids a significant reduction in the wire tension.

The bottom support frame contains high-precision pegholes for PCB-positioning. Layer-spacing control pads were used to ensure the spacing accuracy of each wire layer. The anode was a gold-plated tungsten wire with a diameter of 20  $\mu\text{m}$  and tension of 55 g. The field wire and cathode were composed of gold-plated beryllium copper with a diameter of 100  $\mu\text{m}$  and tension of 150 g. The drift cell was 10 mm  $\times$  10 mm in size. Figure 7d presents a photograph of the inside of the MWDC prototype.

## 4.2 Measurement of the anode wire position accuracy

The accuracy of the anode wire position was measured after fabrication of the prototype. The wire spacing measurement device is shown in Fig. 8a, which mainly includes an optical

microscope, stepping motor to control the movement of the microscope, and a grating scale (resolution better than 1  $\mu\text{m}$ ) for an accurate measurement of the microscope position. Figure 8b presents the distribution of the anode wire spacing for the three layers of the prototype, with standard deviations of 19.9, 17.89, and 14.22  $\mu\text{m}$ , respectively. The gradual reduction in the standard deviation was owing to the gradual optimization of the production process.

## 5 Measurement and optimization of the $^{55}\text{Fe}$ energy spectrum

### 5.1 Distortion of the $^{55}\text{Fe}$ energy spectrum

The 5.9-keV X-rays produced by the  $^{55}\text{Fe}$  are commonly used to test the energy resolution of gas detectors with amplification. After the CEE-MWDC prototype was built, the 5.9-keV X-ray energy spectrum was first measured using commercial electronics, which were manufactured by ORTEC [32]. A 142PC charge-sensitive preamplifier, 572A main amplifier, and ASPEC-927 multichannel analyzer (MCA) were used.

The detector was operated in flow mode with a gas composition of 20%  $\text{CO}_2$  and 80% Ar, and gas pressure of approximately 850 mbar. The operating anode voltage of the detector was +1400 V; the field and cathode wires were grounded. A typical 5.9-keV X-ray energy spectrum of the anode wire layer adjacent to the exit window is shown in Fig. 9a. The energy spectrum of the anode wire layer adjacent to the entrance window demonstrated an even stranger shape, as shown in Fig. 9b. The electric field of the simplified MWDC prototype structure was simulated using COMSOL [33], as shown in Fig. 10a. The simulated conditions were set as follows: field wires, cathode wires, grounded windows, and an anode operating voltage of +1400 V. The results indicated that the electric field intensity in the region between the U-layer cathode and entrance window was approximately 50 V/cm, and that in the region between the V-layer cathode and exit window was approximately 20 V/cm. The 5.9-keV X-rays ionize the gas in the cathode-window region and produce primary electrons. Owing to the leaking electric field in the cathode-window region, certain electrons in this region drift toward the anode wire and generate undesired signals, which distort the energy spectrum. The primary electrons generated in the region between the cathode and window drifted to the anode wires, negatively affecting both the energy and position measurements of the MWDC.

### 5.2 Optimization of the $^{55}\text{Fe}$ energy spectrum

A method that perfectly resolves electric field leakage without changing the electric field inside the drift cell was used

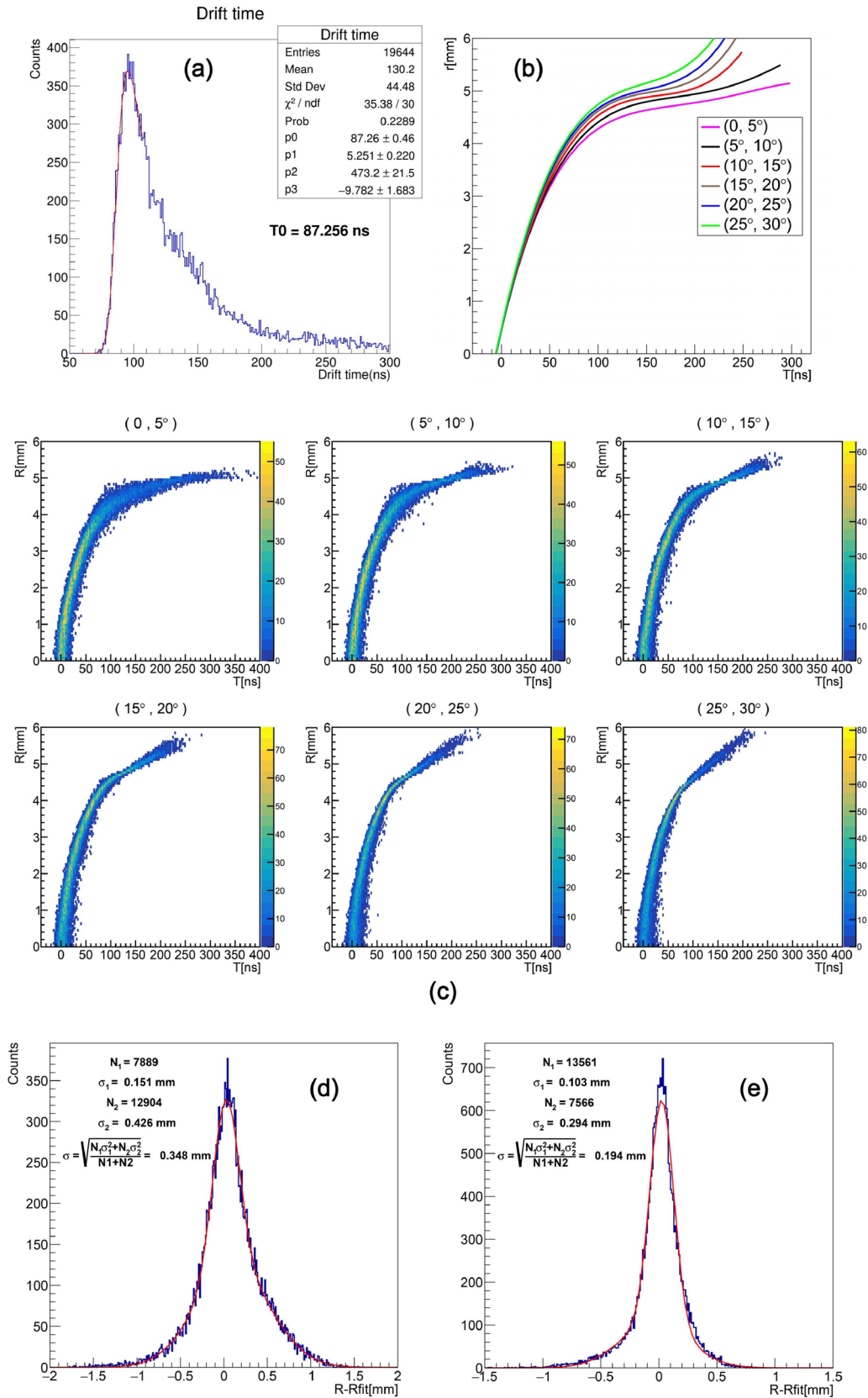


**Fig. 6** (Color online) **a** Drift time spectrum of muons; **b**  $R$ - $T$  functions corresponding to different angle intervals; **c**  $R$ - $T$  correlation plots corresponding to different angle intervals; **d** track residual distribution of muons; **e** track residual distribution of protons

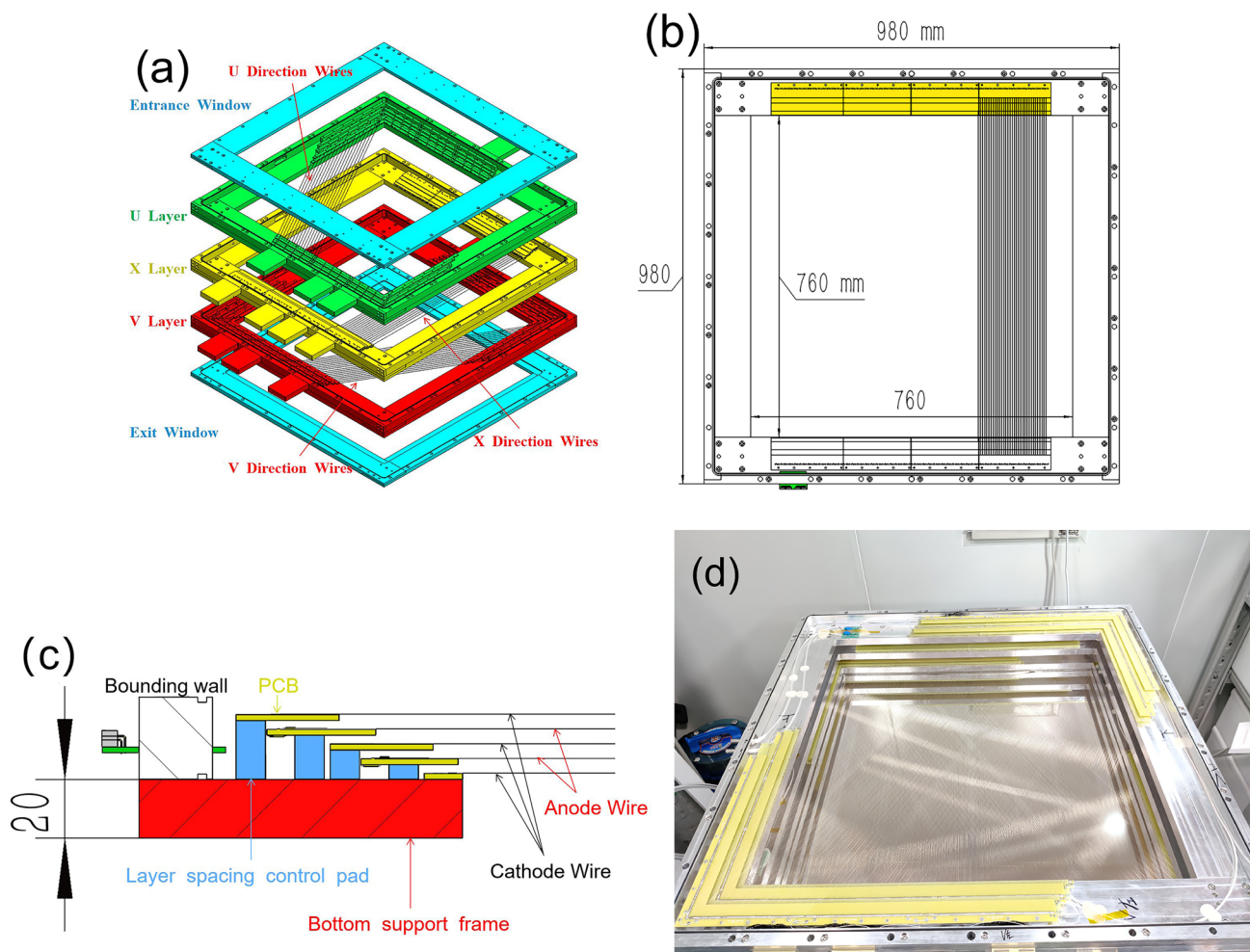


**Fig. 7** (Color online) **a** Schematic diagram of the prototype; **b** top view of the X-measurement layer; **c** cross section of the internal structure of the X-measurement layer; **d** images of the inside of the prototype

to solve the  $^{55}\text{Fe}$ -energy spectrum distortion problem. By changing the voltage configuration of the electrodes, the anode wire voltage of +1400 V, and 0 V of the cathode and field wires, were optimized to an anode wire voltage of +1100 V and cathode and field wire voltage of -300 V. The simulation results for the optimized electric field are shown in Fig. 10b, where the electric field lines in the region between the cathode and window are directed from the window to the cathode. The ionized electrons drift to the window and the ions drift to the cathode wire. Another means to eliminate the undesired signals is to add a layer of guard wire and maintain it at a positive voltage. However, for a large MWDC, the addition of a guard wire layer has two disadvantages: it increases the amount of work required to build it, and the detector structure must withstand a greater wire tension.

The  $^{55}\text{Fe}$ -energy spectrum measured by using the detector after optimizing the voltage configuration is shown in Fig. 9b. The energy spectrum measured by the MWDC

significantly improved by optimizing the voltage configuration. In addition, each cell of the MWDC has distinct boundaries that are beneficial for the overall performance of the detector.

### 5.3 Experimental verification of the distortion principle and optimization mechanism for the $^{55}\text{Fe}$ energy spectrum

To further verify the cause of the energy spectrum distortion by the photoelectric effect of the 5.9-keV X-rays and gas outside the drift cell, a guard wire was placed between the window of the detector and cathode wire for testing.

A schematic of the wire layer structure is shown in Fig. 11a. The field and cathode wires were grounded, and the voltage of the anode wire was +1400 V. The energy spectrum of the  $^{55}\text{Fe}$  source was measured at different guard wire voltages. The experimental results are presented in Fig. 11b. The voltage of the guard wire gradually changed from 0 V to

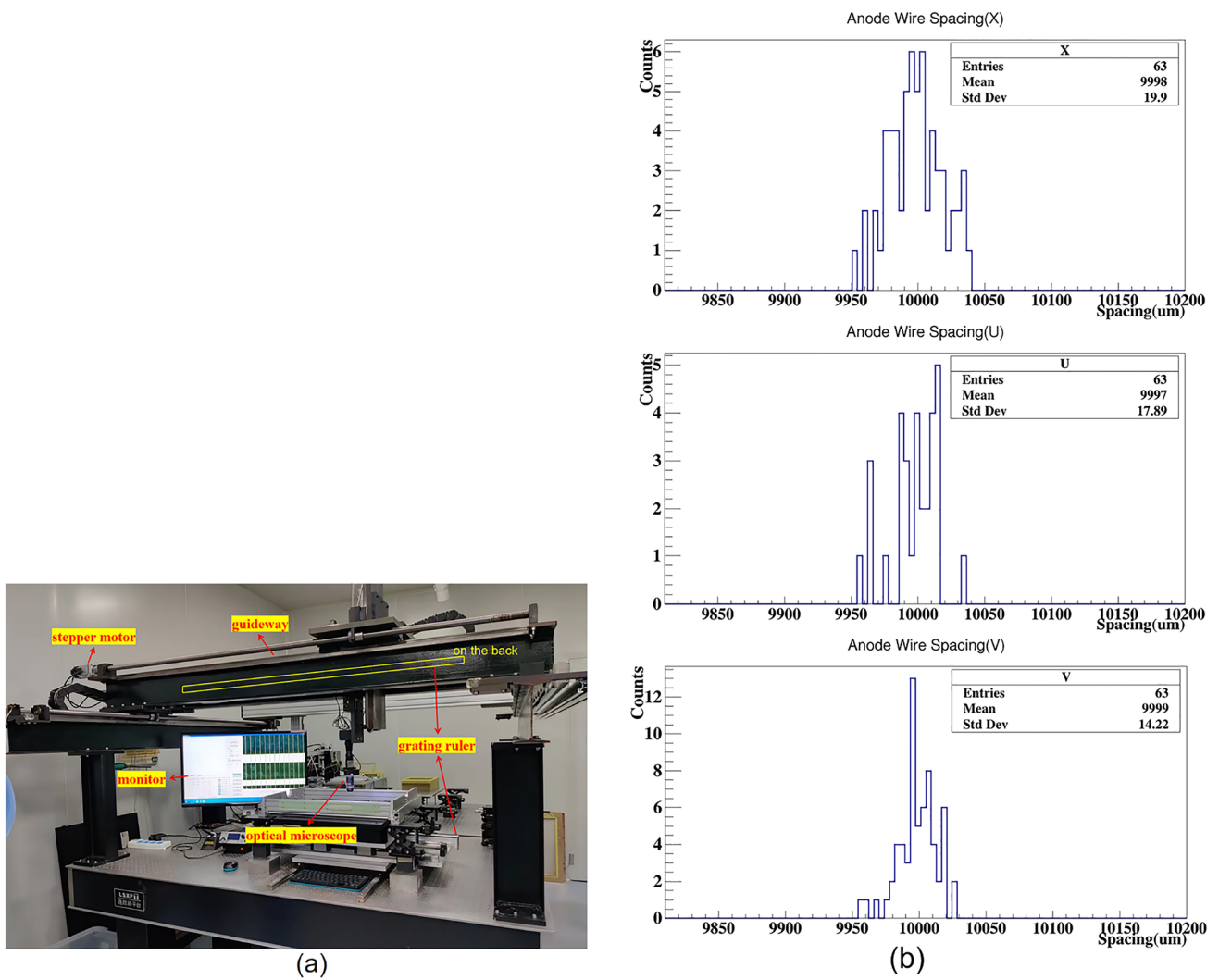


**Fig. 8** **a** Wire spacing measurement device; **b** anode wire spacing distribution of the X-U-V layers

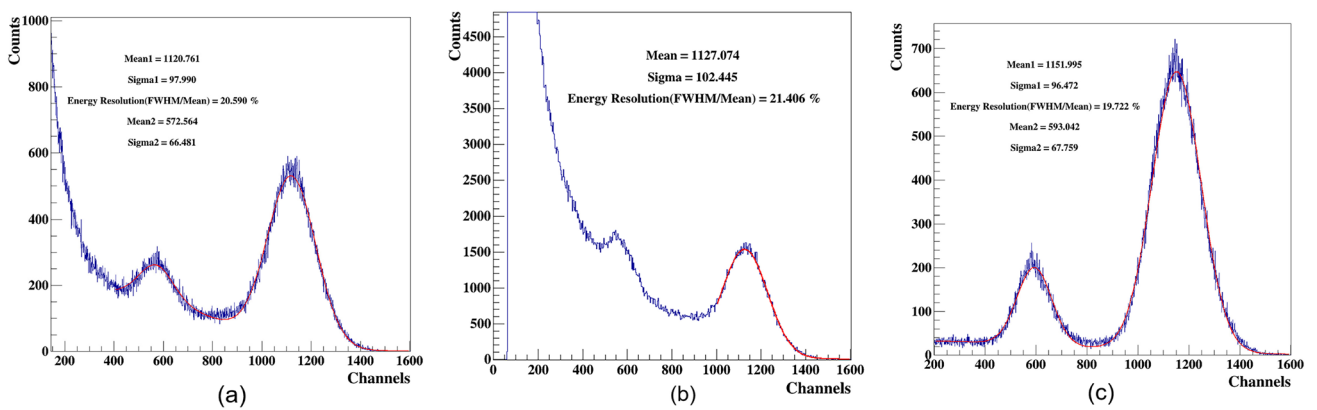


**Fig. 9** Energy spectrum of the anode wire layer adjacent to the **a** exit window and **b** entrance window when the field and cathode wires are grounded (anode wire voltage of +1400 V); **c** typical energy spec-

trum when the field and cathode wire voltage is  $-300$  V, and anode wire voltage is  $+1100$  V

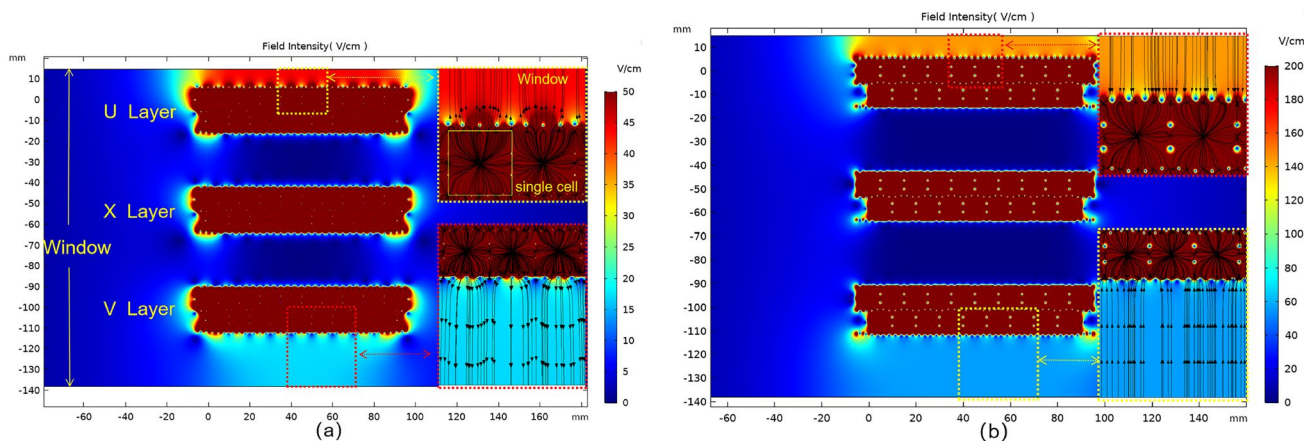


**Fig. 10** (Color online) **a** Distribution of the electric field in the cross section of the prototype when the field and cathode wires are grounded; anode wire voltage is +1400 V; **b** distribution of the elec-

tric field in the cross section of the prototype when the field and cathode wire voltage is -300 V, and anode wire voltage is +1100 V

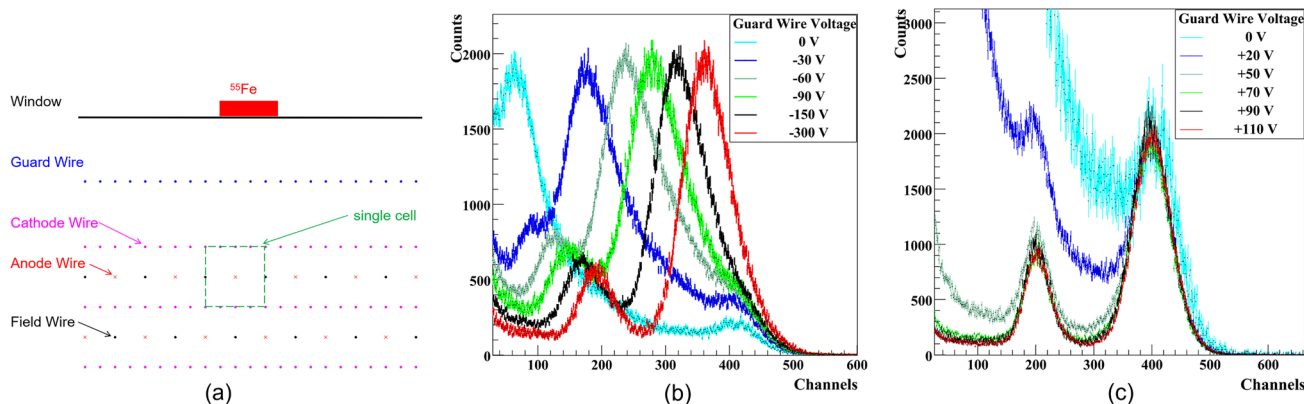


**Fig. 11** (Color online) **a** Schematic diagram of the wire layer structure; variation of the energy spectrum of the  $^{55}\text{Fe}$  source with the guard wire voltage, **b** 0 V to -300 V; **c** 0 V to +110 V

-300 V, and the corresponding level of the main peak of the energy spectrum gradually increased, which was attributed to the ionized electrons external to the drift cell. The 5.9-keV X-rays interacted with the gas between the cathode and guard wires to produce primary electrons, a few of which drifted to the anode wire and generated a signal. The X-ray count between the cathode and guard wires was significantly higher than that inside the drift cell. The voltage of the guard wire gradually changed from 0 V to -300 V. Accordingly, the electric field intensity in the region between the guard wire and cathode wire layers gradually increased, and the direction of the electric field was directed toward the guard wire. As more electrons reached the anode wire, the corresponding main peak of the energy spectrum gradually increased.

As shown in Fig. 11c, the voltage of the guard wire gradually changes from 0 V to +300 V, whereas the electric field

strength between the guard wire and cathode wire layers gradually decrease to zero, followed by a gradual increase. When the voltage of the guard wire was +300 V, the electric field pointed toward the cathode wire layer, and the ionized electrons drifted toward the guard wire. Therefore, the voltage of the guard wire gradually changed from 0 V to +300 V, and it was more difficult for the ionized electrons between the guard wire and cathode wire to drift to the anode wire, reducing the undesired signal.

This study provides a reference for electrode voltage configurations in space-limited wire chamber detectors. Usually, the wire chamber relies on a dense cathode wire as the boundary for the sensitive volume. However, this study found that when the distance between the window and cathode was small, the electric field intensity between the window and cathode wires increased. Using the cathode wires as the boundary of the sensitive volume was no

longer effective, leading to the deterioration of the detector performance. Therefore, a corresponding solution was proposed in this study. Setting the cathode to a negative voltage causes the electrons between the cathode and window to drift toward the window, and the cathode wire forms the effective boundary of the sensitive volume. The results of this study also provide a useful reference for the design of the wire chambers used to measure the particle deposition energy ( $dE$ ). For the  $dE/dx$  measurement, the particle ( $dE$ ) and path length ( $dx$ ) must be clarified.

## 6 Joint testing of the CEE-MWDC detectors and electronics

### 6.1 Position resolution with cosmic rays

The CEE-MWDC detector and electronics were jointly tested to verify that their performances met the CEE requirements. There were 384 detector channels and 192 electronics channels. The detector had six layers of anode wires, each of which selected 32 channels for the signal input electronics. Therefore, the six layers of anode wires overlapped an area of approximately  $800\text{ cm}^2\cdot\text{A}$ ; a block diagram of the electronics used in the experiment is shown in Fig. 12a. Two scintillation detectors were placed in front of and behind

the MWDC. The coincident signals of the two scintillation detectors were used as triggers for SubDAQ. In addition, the signals of the scintillation detector were shaped using an ORTEC 460 amplifier, and the waveform was sampled using the SCA. This was performed to obtain a more accurate relative time-zero value.

The residual distribution of the experimentally measured tracks of the cosmic rays is shown in Fig. 12b, with a sigma value of  $330\text{ }\mu\text{m}$ . The results of the joint tests demonstrate that the scheme satisfies the requirements of the CEE spectrometer.

### 6.2 Energy resolution with the $^{55}\text{Fe}$ source

The energy spectrum of the  $^{55}\text{Fe}$  source was measured using a CEE-MWDC prototype detector in conjunction with the electronics. As shown in Fig. 4b, the energy resolution (FWHM) was approximately 21.3%. The amplitudes of the anode signals were measured at different detector operating voltages, as shown in Fig. 4c. Owing to certain uncontrollable factors, differences between the experimental and simulation results were observed. The energy resolution (FWHM) distributions of the 32 FEE channels are shown in Fig. 12c, with a mean value of 22%. The gain uniformity is illustrated in Fig. 12d, which was less than 4%.

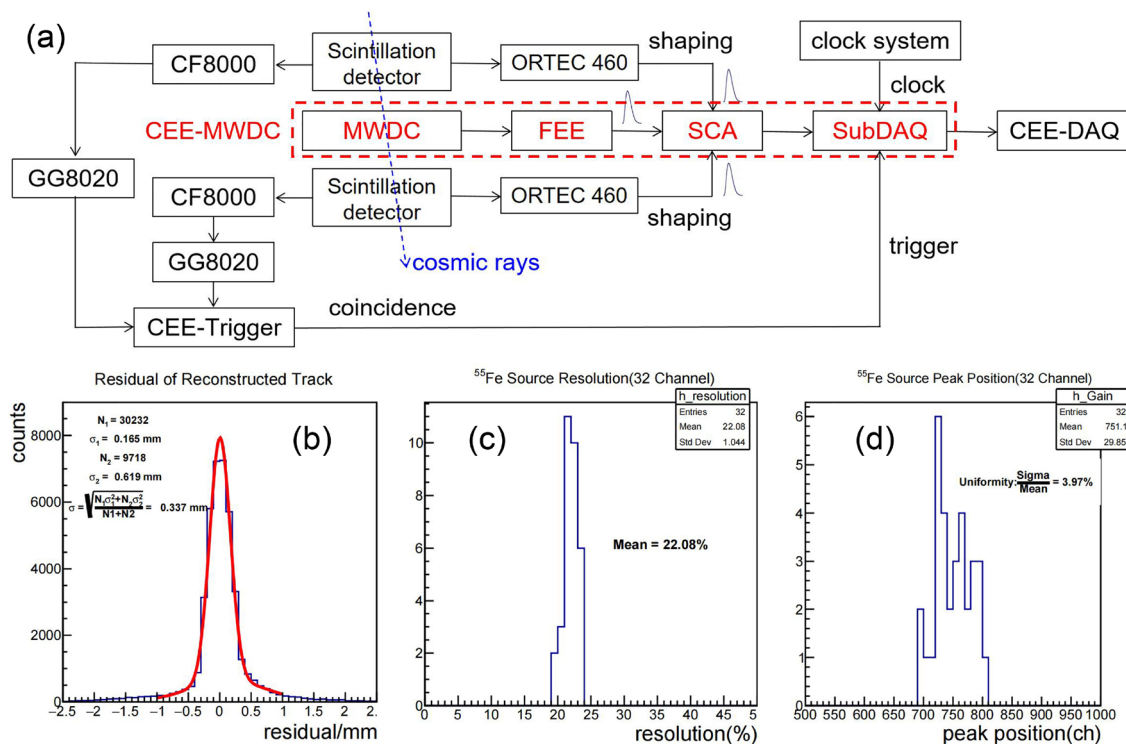


**Fig. 12** **a** Block diagram of the electronic devices used in the experiment; **b** distribution of residuals; **c** distribution of energy resolution (FWHM); **d** distribution of gain

## 7 Conclusion

This study presents a set of Monte Carlo simulation programs based on Garfield++ to simulate the energy and position resolution performance of drift chambers. The program can accurately simulate the ionization process of particles in the gas, electron, and ion transport processes, and the induction signal generation process at the electrodes. The anode-induced current was convolved with the transfer function of specific front-end electronics, and the signal waveform obtained from the simulation was relatively close to the experimental waveform. The amplitude and time information can be extracted from the simulated signal waveforms to analyze the energy and position resolution performances of the MWDC. The program provides a reference for the design of the drift cell of the respective chamber and the setting of important parameters for front-end electronics (e.g., shaping time). It also predicts the detector test conditions, such as the operating voltage and operating gas composition, etc. A half-sized CEE-MWDC prototype was also presented, which demonstrated a standard deviation of less than 20  $\mu\text{m}$  for the position accuracy of the anode wires. This prototype utilized several practical designs to verify its feasibility for the prototype development of large-scale engineering. The detector measured the  $^{55}\text{Fe}$  source energy spectrum using commercial electronics. The energy spectrum of the anode wires near the window was distorted, and a corresponding solution leading to a significant improvement in the energy spectrum was proposed; the energy resolution reached 19.7%. The detector was jointly tested using a self-developed integrated FEE, SCA waveform sampling technique, and an acquisition system. An energy resolution of 22% can be achieved for the 5.9-keV X-rays. The residuals of the measured tracks were 330  $\mu\text{m}$  for the cosmic rays. The performance of the energy and position resolutions met the requirements of CEE.

**Author contributions** All authors contributed to the conception and design of this study. The material preparation, data collection, and analysis were performed by all the authors. The first draft of the manuscript was written by Zhou-Bo He and Zhi Qin. Li-Min Duan, Zhi-Gang Xiao, and Rong-Jiang Hu commented on and revised the previous versions of the manuscript. All the authors have read and approved the final version of the manuscript.

**Data availability** The data that support the findings of this study are openly available in Science Data Bank at <https://cstr.cn/31253.11.sciencedb.08883> and <https://www.doi.org/10.57760/sciencedb.08883>.

## Declarations

**Conflict of interest** The authors declare that they have no conflict of interest.

## References

1. J. Xia, W. Zhan, B. Wei et al., The heavy ion cooler-storage-ring project (HIRFL-CSR) at Lanzhou. Nucl. Inst. Meth. A **488**, 11 (2002). [https://doi.org/10.1016/S0168-9002\(02\)00475-8](https://doi.org/10.1016/S0168-9002(02)00475-8)
2. Y. Yuan, J. Yang, J. Xia et al., Status of the HIRFL-CSR complex. Nucl. Inst. Meth. B **317**, 214 (2013). <https://doi.org/10.1016/j.nimb.2013.07.040>
3. Z. Xiao, L.W. Chen, F. Fu et al., Nuclear matter at a HIRFL CSR energy regime. J. Phys. G Nucl. Partic. **36**, 064040 (2009). <https://doi.org/10.1088/0954-3899/36/6/064040>
4. W. Reisdorf, A. Andronic, R. Averbeck et al., Systematics of central heavy-ion collisions in the 1A GeV regime. Nucl. Phys. A **848**, 366–427 (2010). <https://doi.org/10.1016/j.nuclphysa.2010.09.008>
5. M. Zhang, Z.G. Xiao, S.J. Zhu et al., Systematic studies of the pi-/pi+ ratio with the same neutron/proton ratio but different masses. Phys. Rev. C **80**, 034616 (2009). <https://doi.org/10.1103/PhysRevC.80.034616>
6. L.M. Lü, H. Yi, Z.G. Xiao et al., Conceptual design of the HIRFL-CSR external-target experiment. Sci. China Phys. Mech. Astron. **60**, 012021 (2017). <https://doi.org/10.1007/s11433-016-0342-x>
7. A. Barducci, R. Casalbuoni, G. Pettini et al., A Calculation of the QCD phase diagram at finite temperature and baryon and isospin chemical potentials. Phys. Rev. D **69**, 096004 (2004). <https://doi.org/10.1103/PhysRevD.69.096004>
8. W.D. Myers, W.J. Swiatecki, Nuclear equation of state. Phys. Rev. C **57**, 3020 (1998). <https://doi.org/10.1103/PhysRevC.57.3020>
9. W. Huang, F. Lu, H. Li et al., Laser test of the prototype of CEE time projection chamber. Nucl. Sci. Tech. **29**, 41 (2018). <https://doi.org/10.1007/s41365-018-0382-4>
10. H. Li, S. Zhang, F. Lu et al., Simulation of momentum resolution of the CEE-TPC in HIRFL. Nucl. Tech. (in Chinese) **39**, 70401 (2016). <https://doi.org/10.11889/j.0253-3219.2016.hjs.39.070401>
11. X. Wang, D. Hu, M. Shao et al., CEE inner TOF prototype design and preliminary test results. J. Instrum. **17**, P09023 (2022). <https://doi.org/10.1088/1748-0221/17/09/P09023>
12. L.M. Lyu, H. Yi, L.M. Duan et al., Simulation and prototype testing of multi-wire drift chamber arrays for the CEE. Nucl. Sci. Tech. **31**, 11 (2020). <https://doi.org/10.1007/s41365-019-0716-x>
13. Y.Z. Sun, Z.Y. Sun, S.T. Wang et al., The drift chamber array at the external target facility in HIRFL-CSR. Nucl. Inst. Meth. A **72**, 894 (2018). <https://doi.org/10.1016/j.nima.2018.03.044>
14. H. Yi, Z. Zhang, Z.G. Xiao et al., Prototype studies on the forward MWDC tracking array of the external target experiment at HIRFL-CSR. Chin. Phys. C **38**, 126002 (2014). <https://doi.org/10.1088/1674-1137/38/12/126002>
15. B. Wang, D. Han, Y. Wang et al., The CEE-eTOF wall constructed with new sealed MRPC. J. Instrum. **15**, C08022 (2020). <https://doi.org/10.1088/1748-0221/15/08/C08022>
16. B. Wang, X.L. Chen, Y. Wang et al., A simulation and analysis framework for CEE-eTOF. J. Instrum. **17**, P07024 (2022). <https://doi.org/10.1088/1748-0221/17/07/P07024>
17. S. Zhu, H. Yang, H. Pei et al., Prototype design of readout electronics for zero degree calorimeter in the HIRFL-CSR external-target experiment. J. Instrum. **16**, P08014 (2021). <https://doi.org/10.1088/1748-0221/16/08/p08014>
18. L.K. Liu, H. Pei, Y.P. Wang et al., Event plane determination from the zero degree calorimeter at the cooling storage ring external target experiment. Nucl. Sci. Tech. **34**, 100 (2023). <https://doi.org/10.1007/s41365-023-01262-8>
19. D. Hu, X. Wang, M. Shao et al., Beam test study of the MRPC-based T0 detector for the CEE. J. Instrum. **14**, C09030 (2019). <https://doi.org/10.1088/1748-0221/14/09/C09030>
20. D.D. Hu, J.M. Lu, J. Zhou et al., Extensive beam test study of prototype MRPCs for the T0 detector at the CSR external-target

- experiment. *Eur. Phys. J. C* **80**, 282 (2020). <https://doi.org/10.1140/epjc/s10052-020-7804-2>
21. H.L. Wang, Z. Wang, C.S. Gao et al., Design and tests of the prototype beam monitor of the CSR external target experiment. *Nucl. Sci. Tech.* **33**, 36 (2022). <https://doi.org/10.1007/s41365-022-01021-1>
  22. B. You, C. Gao, P. Yang et al., The Topmetal-CEE prototype, a direct charge sensor for the beam monitor of the CSR external-target experiment. *J. Instrum.* **17**, C09030 (2022). <https://doi.org/10.1088/1748-0221/17/09/C09030>
  23. J. Liu, C.S. Gao, H.L. Wang et al., Design and preliminary characterization of a novel silicon charge sensor for the gaseous beam monitor at the CSR external-target experiment. *Nucl. Inst. Meth. A* **1047**, 167786 (2023). <https://doi.org/10.1016/j.nima.2022.167786>
  24. D. Guo, X. He, P. Li et al., Studies of nuclear equation of state with the HIRFL-CSR external-target experiment. *Eur. Phys. J. A* **60**, 36 (2024). <https://doi.org/10.1140/epja/s10050-024-01245-2>
  25. H. Schindler, "Garfield++." <http://garfieldpp.web.cern.ch/garfieldpp>
  26. I.B. Smirnov, Modeling of ionization produced by fast charged particles in gases. *Nucl. Inst. Meth. A* **554**, 474–493 (2005). <https://doi.org/10.1016/j.nima.2005.08.064>
  27. S. Biagi, "Magboltz." <http://magboltz.web.cern.ch/magboltz/>
  28. S. Biagi, "Magboltz 11.17." <https://magboltz.web.cern.ch/magboltz/magboltz-11.17.f>
  29. K. Malinowski, M. Chernyshova, T. Czarski et al., Simulation of energy spectrum of GEM detector from an x-ray quantum. *J. Instrum.* **13**, C01018 (2018). <https://doi.org/10.1088/1748-0221/13/01/C01018>
  30. D.S. Levin, N. Amram, R. Ball et al., Drift time spectrum and gas monitoring in the ATLAS Muon Spectrometer precision chambers. *Nucl. Inst. Meth. A* **588**, 347–358 (2008). <https://doi.org/10.1016/j.nima.2008.01.096>
  31. J.B. Liu, Z.H. Qin, L.H. Wu et al., A beam test of a prototype of the BESIII drift chamber in magnetic field. *Nucl. Inst. Meth. A* **557**, 436–444 (2006). <https://doi.org/10.1016/j.nima.2005.11.093>
  32. "ORTEC." <https://ortec.com>
  33. "COMSOL — software for multiphysics simulation." <https://cn.comsol.com>

Springer Nature or its licensor (e.g. a society or other partner) holds exclusive rights to this article under a publishing agreement with the author(s) or other rightsholder(s); author self-archiving of the accepted manuscript version of this article is solely governed by the terms of such publishing agreement and applicable law.